

Unified description of fluids and solids in Smoothed Particle Hydrodynamics

Ondřej Kincl^{a,*}, Ilya Peshkov^b, Michal Pavelka^a and Václav Klika^c

^aMathematical Institute, Faculty of Mathematics, Charles University, Sokolovská 83, Prague, 186 75, Czech Republic

^bUniversity of Trento, Department of Civil, Environmental and Mechanical Engineering, Via Mesiano 77, Trento, 38123, Italy

^cCzech Technical University in Prague, Dept. of Mathematics, FNSPE, Trojanova 13, Prague, 120 00, Czech Republic

ARTICLE INFO

Keywords:

SPH
SHTC
solid mechanics
fluid dynamics
energy-conservation
tensile instability

ABSTRACT

Smoothed Particle Hydrodynamics (SPH) methods are advantageous in simulations of fluids in domains with free boundary. Special SPH methods have also been developed to simulate solids. However, there are situations where the matter behaves partly as a fluid and partly as a solid, for instance, the solidification front in 3D printing, or any system involving both fluid and solid phases. We develop an SPH-like method that is suitable for both fluids and solids at the same time. Instead of the typical discretization of hydrodynamics, we discretize the Symmetric Hyperbolic Thermodynamically Compatible equations (SHTC), which describe both fluids, elastic solids, and visco-elasto-plastic solids within a single framework. The resulting SHTC-SPH method is then tested on various benchmarks from the hydrodynamics and dynamics of solids and shows remarkable agreement with the data.

Contents

1	Introduction	1
2	Governing PDEs	2
3	The SHTC-SPH Method	3
3.1	Discrete density	4
3.2	Discrete distortion	4
3.3	Reversible part of the SHTC-SPH equations	5
3.4	Constitutive equations	7
3.5	Tensile penalty	7
3.6	Time integrator	9
3.7	Adding relaxation	10
4	Numerical results	11
4.1	Beryllium plate	11
4.2	Twisting column	12
4.3	Laminar Taylor-Couette flow	15
4.4	Lid-driven cavity (Newtonian fluid)	17
5	Conclusion	19

1. Introduction

We continue investigating different numerical strategies for the discretization of the unified formulation of continuum fluid and solid mechanics [34, 10], which can describe flows of Newtonian and non-Newtonian fluids [32], as well

*Corresponding author

✉ ondrej.kincl.6@gmail.com (O. Kincl); ilya.peshkov@unitn.it (I. Peshkov); pavelka@karlin.mff.cuni.cz (M. Pavelka); vavclav.klika@cvut.cz (V. Klika)

ORCID(s): 0000-0001-8285-0639 (I. Peshkov); 0000-0003-0605-6737 (M. Pavelka)

as deformations of elastoplastic solids [31] in a single system of first-order hyperbolic partial differential equations. In this paper, we are particularly interested in the capabilities of the Smoothed Particle Hydrodynamics approach to capture the solution to the unified model in both fluid and solid regimes. Because the non-dissipative part of the model (all differential terms) belongs to the class of Symmetric Hyperbolic Thermodynamically compatible (SHTC) equations [33, 35, 17, 15, 16], we shall also refer to the unified model as the SHTC equations. Moreover, as shown in [33] the SHTC equations can also be seen as a particular realization of the GENERIC (General Equation for Non-Equilibrium Reversible-Irreversible Coupling) approach [18, 27, 28] to non-equilibrium thermodynamics. In the long-term perspective, we, therefore, are interested in developing an SPH Hamiltonian integrator that respects various properties of the continuous equations (differential constraints, Jacobi identity, etc.) at the discrete level. This goal is partially addressed in this paper.

Previously, the unified model of continuum mechanics was discretized using various *mesh-based* techniques including Godunov-type finite volume methods and Discontinuous Galerkin methods [10], Arbitrary Lagrangian Eulerian methods [31, 7], a finite volume methods in the Updated Lagrangian formulation with a high-order IMEX time integrator [4], semi-implicit staggered finite volume method [5] for low-Mach problems, thermodynamically compatible finite volume scheme [8].

This time, we turn to the discretization of the SHTC equations with *mesh-free* methods and, in particular, with the Smoothed Particle Hydrodynamics (SPH), which is a particle-based numerical method for partial differential equations introduced by Gingold and Monaghan in 1977 [14]. The method allows for an elegant treatment of complex time-dependent geometries. This feature makes it attractive for problems involving fluid-structure interactions [2] and multiphase flows [25]. Despite its name, the method is also applicable to solids [22]. We refer, for example, to [24] for a comprehensive review.

Although SPH methods were successfully applied to simulate fluids and solids, the schemes and equations were rather different. For example, fluid mechanics equations are formulated in the Eulerian frame, while solid mechanics equations are traditionally formulated in the Lagrangian frame. Our ultimate goal, therefore, to develop a single reliable scheme that works in both fluid and solid regimes of the SHTC equations, is far from being trivial. For example, such a goal is very appealing from the perspective of modeling material flows that exhibit coexistence of the fluid and solid states, as well as mutual transformations, e.g. selective laser metal printing (3D printing of metals), flows of viscoplastic fluids, granular flows [1], landslides and avalanches, ice formation, etc.

Despite the fact that the SHTC equations are formulated in the Eulerian frame (which is necessary for a fluid-like motion), these equations also have a particle-like, and therefore Lagrangian, nature, which was discussed in [9]. In particular, the main field of SHTC equations that makes it possible to describe fluids and solids at once is the distortion field \mathbb{A} . Distortion can be seen as a field of infinitesimal local basis triads, which are allowed to arbitrary rearrange with their neighbors and thus exhibit the particle-like nature. Such a continuum description of matter was in particular inspired by Frenkel's idea to characterize the fluidity of the liquids by the so-called characteristic particle rearrangement time τ [12, 6]. Moreover, the SHTC equations can be derived by the transformation of the Lagrangian Hamiltonian continuum mechanics to the Eulerian continuum [29]. Due to such a particle-like nature of the SHTC equations and the freedom in the rearrangements of the infinitesimal material elements, the mesh-based methods can not completely capture the microscopic dynamics of the SHTC equations, but it can only be revealed with a particle-based method, e.g. SPH.

The numerical scheme proposed in this paper is based on an explicit variant of SPH. First, we perform the spatial semidiscretization of the reversible part of the SHTC system. The exact form of discrete operators is derived from a potential, which guarantees the conservation of energy. We obtain a system of ordinary differential equations, for which we find an efficient time-reversible integrator. We also discuss the problem of tensile instability and suggest a solution without interfering with the conservative properties of SPH. Finally, the irreversible part is added using the Runge-Kutta scheme as time integrator. The last section is devoted to the validity tests.

2. Governing PDEs

The unified model of continuum fluid and solid mechanics is formulated in the Eulerian frame in a Cartesian coordinate system $\mathbf{x} = \{x_1, x_2, x_3\}$ as follows [34, 10]

$$\frac{\partial \rho}{\partial t} + \nabla \cdot (\rho \mathbf{v}) = 0, \quad (1a)$$

$$\frac{\partial(\rho \mathbf{v})}{\partial t} + \nabla \cdot (\mathbf{v} \otimes \rho \mathbf{v} - \mathbb{S}) = 0, \quad (1b)$$

$$\frac{\partial \mathbb{A}}{\partial t} + \mathbf{v} \cdot \nabla \mathbb{A} + \mathbb{A} \nabla \mathbf{v} = -\frac{1}{\theta} E_{\mathbb{A}}, \quad (1c)$$

$$\frac{\partial(\rho E)}{\partial t} + \nabla \cdot (\mathbf{v} \rho E - \mathbb{S} \mathbf{v}) = 0, \quad (1d)$$

where ρ is the mass density of the material, $\mathbf{v} = \{v_1, v_2, v_3\}$ is the velocity field, $\mathbf{v} \otimes \rho \mathbf{v} = \{\rho v^i v^j\}$, $\mathbb{A} = \{A^{ij}\}$ is the distortion field, $\nabla \mathbf{v} = \{\frac{\partial v^i}{\partial x^j}\}$, $\mathbf{v} \cdot \nabla = v^i \frac{\partial}{\partial x^i}$, $\mathbb{S} = \{S^{ij}\}$ is the total stress tensor whose specification depends on the material under consideration and is defined by the total energy density specification $E = E(\rho, \mathbf{v}, \mathbb{A}) = \epsilon(\rho, \mathbb{A}) + \frac{1}{2} \|\mathbf{v}\|^2$, see Section 3.4. In addition, $\epsilon(\rho, \mathbb{A})$ is the internal energy that must be specified by the user.

The left-hand side of the equations is the reversible part of the time evolution and can be derived either from the variational principle or can be generated by Poisson brackets [33]. This part describes the elasticity of the material. The right-hand side is characterized by the relaxation term in the distortion equation. Here, $E_{\mathbb{A}} = \frac{\partial E}{\partial \mathbb{A}}$ and is essentially the Lagrangian stress tensor (first Piola-Kirchhoff stress), while the scalar $\theta = \theta(\rho, \tau, \mathbb{A}) \geq 0$ is a relaxation function which depends on the state variables and some material constants. In particular, $\theta \sim \tau$, where τ is the strain relaxation time and one of the key elements of the SHTC model to describe fluids and solids. For example, in this framework, fluids can be seen as the relaxation limit (small relaxation time $0 < \tau \ll \infty$) of a solid when the shear stresses are strongly relaxed (“melted” solid). For Newtonian fluids τ can be taken constant, while for non-Newtonian fluids and elastoplastic solids τ is the function of the stress state [32, 31], and therefore of the distortion field $\tau = \tau(\mathbb{A})$ (as well as other parameters, e.g. temperature). For simplicity, we ignore the heat transfer effect which is also described by hyperbolic relaxation equations in the SHTC framework [5, 33, 28], as well as the materials are considered as isothermal. The heat conduction will be included in a follow up paper.

The following section contains a numerical method (SHTC-SPH) that finds approximate solutions of the SHTC equations (1) in both the fluid and solid regimes.

3. The SHTC-SPH Method

In order to address the SHTC equations (1), which contain the distortion field (unlike hydrodynamics), we have to define a discrete analogy of the continuous distortion. But before that, let us first recall the standard construction of SPH via smoothing kernels.

The SPH is based on *smoothing kernels* to calculate the influence of a particle on its surroundings. In this paper, we will use Wendland’s quintic kernel, which reads

$$w(r) = \begin{cases} \frac{\alpha_d}{h^d} \left(1 - \frac{r}{2h}\right)^4 \left(1 + \frac{2r}{h}\right), & r \leq 2h \\ 0, & r \geq 2h \end{cases} \quad (2)$$

where r is the distance from the center of the particle, h is the *smoothing length* and d is the dimension. The constant α_d has the following values:

$$\begin{cases} \alpha_2 = \frac{7}{4\pi} \\ \alpha_3 = \frac{21}{16\pi} \end{cases}.$$

Following Violeau [38], we will use the notation

$$w_{ab} = w(r_{ab}), \quad w'_{ab} = \frac{dw}{dr}(r_{ab})$$

where $r_{ab} = |\mathbf{x}_a - \mathbf{x}_b| = |\mathbf{x}_{ab}|$ is the distance between two particles with positions $\mathbf{x}_a, \mathbf{x}_b$ in the Eulerian frame. Furthermore, let us also denote

$$\nabla w_{ab} = w'_{ab} \frac{\mathbf{x}_{ab}}{r_{ab}}.$$

Realizing that

$$\frac{w'(r)}{r} = \begin{cases} -\frac{10\alpha_d}{h^{d+1}} \left(1 - \frac{r}{2h}\right)^3, & r \leq 2h \\ 0, & r \geq 2h \end{cases} \quad (3)$$

we can implement ∇w_{ab} in a way that avoids potential division by $r = 0$.

Moreover, in the initial state, the particles are placed in a regular pattern, filling a domain Ω_0 such that every particle occupies a volume $V_0 = \delta r^d$, where $\delta r > 0$ is the spatial step of the simulation. In the 2D case, an isometric grid arrangement is used in this paper, while in the 3D case, the particles are initially distributed in a body-centered cubic crystal. We can now proceed to the definition of the discrete state variables.

3.1. Discrete density

Mass density can be approximated, using interpolation by smoothing kernel density ρ_a at \mathbf{x}_a , as

$$\rho_a = \sum_b m_b w_{ab} + C_{\rho,a} \quad (4)$$

where $C_{\rho,a}$ is a time-independent parameter that enforces the equality of ρ_a with the reference density ρ_0 at the initial time instant $t = 0$ (this is necessary to obtain the vanishing internal energy of the free surface particles). We assume that the masses of the particles m_b are positive and do not depend on time [21]. In all the examples presented in this paper, we use $m_b = \rho_0 V_0 \big|_b$ where the volume of the particles follows from $V_a = (\sum_b w_{ab})^{-1}$.

A straightforward computation then yields the following formula for the differential of the discrete density.

Statement 1. Assuming $r_{ab} > 0$ for each pair of particles, the total differential of ρ_a according to formula (4) with respect to the positions of the particles \mathbf{x} is

$$d\rho_a = \sum_b m_b d\mathbf{x}_{ab} \cdot \nabla w_{ab} \quad (5)$$

3.2. Discrete distortion

An important variable in the SHTC equations is the *distortion* matrix. In the reversible (elastic) case, when it can be thought of as the inverse of the deformation tensor, it satisfies the following equation [28, Chap 3]

$$\dot{\mathbb{A}} = -\mathbb{A}\mathbb{L}, \quad (6)$$

where \mathbb{L} is the velocity gradient and the dot denotes the material time derivative. Using a renormalized SPH gradient [3, 37] inspired by a work by Falk and Langer [11], we can approximate this quantity as

$$\mathbb{L}_a = \left(\sum_b m_b \mathbf{v}_{ab} \otimes \nabla w_{ab} \right) \left(\sum_b m_b \mathbf{x}_{ab} \otimes \nabla w_{ab} \right)^{-1}. \quad (7)$$

The following statement explains that \mathbb{L}_a can be found by approximating a differential formula $d\mathbf{v} = \mathbb{L} d\mathbf{x}$:

Statement 2. Assume $r_{ab} > 0$ for each pair of particles and for any fixed particle a that there are d linearly independent vectors \mathbf{x}_{ab} satisfying $r_{ab} < 2h$. (In other words, particle a and its neighbors must not be co-planar in 3D or co-linear in 2D.) Then the matrix inverse in (7) exists and \mathbb{L}_a is the unique solution of the overdetermined system

$$\mathbb{L}_a \mathbf{x}_{ab} \doteq \mathbf{v}_{ab}$$

in the sense of weighted least squares with weights $m_b \frac{|w'_{ab}|}{r_{ab}}$.

Proof. Note that $|w'_{ab}| = -w'_{ab}$. It is clear from the assumptions that the matrix

$$-\sum_b m_b \mathbf{x}_{ab} \otimes \nabla w_{ab} = \sum_b \frac{m_b |w'_{ab}|}{r_{ab}} (\mathbf{x}_{ab} \otimes \mathbf{x}_{ab})$$

is positive definite and thus invertible. Now, the global minimum of coercive and differentiable function

$$\mathcal{E}(\mathbb{L}_a) = -\frac{1}{2} \sum_b m_b \frac{w'_{ab}}{r_{ab}} |\mathbb{L}_a \mathbf{x}_{ab} - \mathbf{v}_{ab}|^2$$

with respect to \mathbb{L}_a exists and satisfies

$$\begin{aligned} 0 &= d\mathcal{E}_a = - \sum_b m_b \frac{w'_{ab}}{r_{ab}} (\mathbb{L}_a \mathbf{x}_{ab} - \mathbf{v}_{ab}) \cdot d\mathbb{L}_a \mathbf{x}_{ab} \\ &= -d\mathbb{L}_a : \sum_b m_b (\mathbb{L}_a \mathbf{x}_{ab} - \mathbf{v}_{ab}) \otimes \nabla w_{ab}, \quad \forall d\mathbb{L}_a. \end{aligned}$$

This immediately yields (7). □

As a corollary of Statement 2, it is clear that the definition (7) is first-order exact. In fact, $\mathbb{L}_a \mathbf{x}_{ab} = \mathbf{v}_{ab}$ will be solved exactly by least squares, provided that there is an exact solution, which occurs exactly when \mathbf{v} can be written as a linear function of \mathbf{x} .

Combining (6) with (7), we obtain the evolution of \mathbb{A}_a in the form

$$\dot{\mathbb{A}}_a = -\mathbb{A}_a \left(\sum_b m_b \mathbf{v}_{ab} \otimes \nabla w_{ab} \right) \left(\sum_b m_b \mathbf{x}_{ab} \otimes \nabla w_{ab} \right)^{-1}. \quad (8)$$

We can rephrase this using a linear form that relates changes of \mathbb{A}_a to variations of \mathbf{x}_a :

$$d\mathbb{A}_a = -\mathbb{A}_a \left(\sum_b m_b d\mathbf{x}_{ab} \otimes \nabla w_{ab} \right) \left(\sum_b m_b \mathbf{x}_{ab} \otimes \nabla w_{ab} \right)^{-1}, \quad (9)$$

which defines \mathbb{A}_a provided that its initial value is specified and the particle trajectories are known. Here, we have a subtle problem because we do not have any guarantee that the right-hand side in (9) is integrable. Therefore, when Γ is a closed loop in the configuration space, we, in general, have the following

$$\int_{\Gamma} d\mathbb{A}_a \neq 0.$$

In other words, if (9) is used, the numerical distortion may not recover when the shape of a material does, potentially introducing some artificial irreversibility. Without resorting to the Lagrangian description, we have not found a satisfactory solution to this problem in pure Eulerian settings.

On a side note, instead of treating the density as a separate variable, it is possible to use

$$\rho_a = \rho_0 \det \mathbb{A}_a.$$

However, in our numerical experience, using formula (4) is more reliable.

3.3. Reversible part of the SHTC-SPH equations

Let us now consider the case of an elastic solid with internal energy

$$\mathcal{U} = \int_{\Omega} \rho \epsilon dx.$$

which we discretize as

$$\mathcal{U}_h = \sum_a m_a \epsilon_a,$$

where $\epsilon_a = \epsilon(\rho_a, \mathbb{A}_a)$ is the specific internal energy. For simplicity of notation, let us write

$$\begin{aligned}\mathbb{H}_a &= \sum_b m_b \mathbf{x}_{ab} \otimes \nabla w_{ab} \\ \mathbb{T}_a &= -\epsilon_{\rho_a} \mathbb{I} + \mathbb{A}_a^T \epsilon_{\mathbb{A}_a} \mathbb{H}_a^{-1},\end{aligned}\tag{10}$$

where we employed the usual notation for partial derivatives $\epsilon_{\rho_a} = \frac{\partial \epsilon}{\partial \rho_a}$, $\epsilon_{\mathbb{A}_a} = \frac{\partial \epsilon}{\partial \mathbb{A}_a}$. Now, using (5), (9), we find how \mathcal{U} varies when \mathbf{x} changes:

$$\begin{aligned}d\mathcal{U}_h &= \sum_a m_a \epsilon_{\rho_a} d\rho_a + \sum_a m_a \epsilon_{\mathbb{A}_a} : d\mathbb{A}_a \\ &= \sum_{a,b} m_a m_b \left(\epsilon_{\rho_a} \nabla w_{ab} \cdot d\mathbf{x}_{ab} - \epsilon_{\mathbb{A}_a} : \mathbb{A}_a (d\mathbf{x}_{ab} \otimes \nabla w_{ab}) \mathbb{H}_a^{-1} \right) \\ &= - \sum_{a,b} m_a m_b \mathbb{T}_a \nabla w_{ab} \cdot d\mathbf{x}_{ab} \\ &= - \sum_{a,b} m_a m_b (\mathbb{T}_a + \mathbb{T}_b) \nabla w_{ab} \cdot d\mathbf{x}_a.\end{aligned}\tag{11}$$

Combining (8), (11) and $m_a \dot{\mathbf{v}}_a = -\frac{\partial \mathcal{U}_h}{\partial \mathbf{x}_a}$ (Newton's law), we obtain a system of ordinary differential equations:

$$\begin{aligned}\dot{\mathbf{x}}_a &= \mathbf{v}_a \\ \dot{\mathbf{v}}_a &= \sum_b m_b (\mathbb{T}_a + \mathbb{T}_b) \nabla w_{ab} \\ \dot{\mathbb{A}}_a &= -\mathbb{A}_a \mathbb{L}_a,\end{aligned}\tag{12}$$

which is the system of the SHTC-SPH ordinary differential equations approximating the SHTC equations.

One of the greatest assets of SHTC-SPH is that it enjoys various conservative properties.

Statement 3. *The system of equations (12) satisfies the conservation of the*

- energy

$$\mathcal{H}_h = \sum_a m_a \left(\frac{v_a^2}{2} + \epsilon_a \right),$$

- linear momentum

$$\mathcal{M}_h = \sum_a m_a \mathbf{v}_a,$$

- angular momentum (provided that the shear stress tensor $\mathbb{A}_a^T \epsilon_{\mathbb{A}_a}$ is symmetric)

$$\mathcal{L}_h = \sum_a m_a \mathbf{x}_a \times \mathbf{v}_a.$$

Proof. Conservation of energy follows from the construction, linear momentum is conserved due to antisymmetry $\nabla w_{ab} = -\nabla w_{ba}$. Likewise, showing conservation of angular momentum is easy because

$$\begin{aligned}\dot{\mathcal{L}}_h^i &= \epsilon^{ijk} \sum_a m_a x_a^j \dot{v}_a^k \\ &= \epsilon^{ijk} \sum_a m_a x_a^j \left(\sum_b m_b (T_a^{kl} + T_b^{kl}) \nabla_{ab} w^l \right) \\ &= \epsilon^{ijk} \sum_a m_a T_a^{kl} \left(\sum_b m_b x_{ab}^i \nabla_{ab} w^l \right) \\ &= \epsilon^{ijk} \sum_a m_a T_a^{kl} H_a^{li} \\ &= 0\end{aligned}$$

since the matrix $\mathbb{T}_a \mathbb{H}_a$ is symmetric. □

3.4. Constitutive equations

The set of equations (12) is incomplete until one specifies the dependence of internal energy ϵ on ρ, \mathbb{A} . In this paper, we assume the decomposition of energy into the bulk and shear components:

$$\epsilon(\rho, \mathbb{A}) = \epsilon_0(\rho) + \epsilon_s(\mathbb{A}).$$

For the bulk energy component, we can use a simple quadratic relation

$$\epsilon_0(\rho) = \frac{c_0^2}{2} \left(\frac{\rho_0}{\rho} - 1 \right)^2. \quad (13)$$

where c_0 is the bulk speed of sound. This choice is not unique but serves well for the demonstration purposes. Alternatives exist (see, e.g. [28]), but the distinction is typically less important for materials which are difficult to compress. From (13), we can deduce a formula for the pressure:

$$p = \rho^2 \frac{\partial \epsilon_0}{\partial \rho} = c_0^2 \rho_0 \left(1 - \frac{\rho_0}{\rho} \right). \quad (14)$$

For the shear elastic energy, we consider two variants. Following the papers [10], we can use

$$e_s^{DPRZ}(\mathbb{A}) = \frac{c_s^2}{4} \|\text{dev}(\mathbb{A}^T \mathbb{A})\|_F^2, \quad (15)$$

where c_s is the shear speed of sound, $\|\cdot\|_F$ is the Frobenius norm and

$$\text{dev } \mathbb{M} = \mathbb{M} - \frac{1}{3}(\text{tr } \mathbb{M}) \mathbb{I}$$

denotes *deviatoric part*. Plugging this into (10), we get

$$\mathbb{T}_a = -\frac{p_a}{\rho_a^2} \mathbb{I} + c_s^2 \mathbb{A}_a^T \mathbb{A}_a \text{dev}(\mathbb{A}_a^T \mathbb{A}_a) \mathbb{H}_a^{-1}. \quad (16)$$

Although less convenient in the Eulerian setting, it is also possible to use the Neo-Hookean model

$$e_s^{NH}(\mathbb{A}) = \frac{c_s^2}{2} (\text{tr } \mathbb{B}_a - 3 + 2 \ln \det \mathbb{A}_a), \quad (17)$$

which yields:

$$\mathbb{T}_a = -\frac{p_a}{\rho_a^2} \mathbb{I} - c_s^2 (\mathbb{B}_a - \mathbb{I}) \mathbb{H}_a^{-1}, \quad (18)$$

with $\mathbb{B}_a = \mathbb{A}_a^{-T} \mathbb{A}_a^{-1}$ being the left Cauchy-Green tensor and the pressure in a particle follows from (14) as

$$p_a = c_0^2 \rho_0 \left(1 - \frac{\rho_0}{\rho_a} \right).$$

3.5. Tensile penalty

A common issue encountered in SPH is the *tensile instability* — a numerical artifact, which causes unwanted clumping of particles in regions of negative pressure. Due to non-linearities in formula (4), density ρ will increase slightly under tensile strain. This is usually not a problem for $p > 0$, however, for $p < 0$ particles can reduce their potential by tensile strain according to

$$\frac{\partial \epsilon}{\partial \rho} = \frac{p}{\rho^2}.$$

This often results in the formation of particle chains surrounded by void patches, which can eventually cause body tearing. There are a few remedies offered in the literature. Paper [26] recommends adding an artificial force that repels particles with abnormally small separation. Another possible treatment, called δ -shifting [36], subjects the particles to artificial diffusion. In this paper, we suggest adding the following *tensile penalty* term to the energy:

$$\mathcal{P}_h = \frac{1}{2} \sum_a m_a c_p^2 \left(\frac{\lambda_a}{\rho_0} \right)^2, \quad (19)$$

where c_p is a numerical parameter with velocity dimensions that determines the strength of anti-clumping forces. The variable λ_a is defined by the relation

$$\lambda_a = h \frac{\partial \rho_a}{\partial h} + C_{\lambda,a} = \sum_b m_b h \frac{\partial w_{ab}}{\partial h} + C_{\lambda,a}. \quad (20)$$

Our idea is to describe clustering as a situation where ρ_a increases when we take a smaller smoothing length h . By adding this energy term, we enforce a nice structure of the particles by keeping $\frac{\partial \rho_a}{\partial h}$ small. Similarly to (4), we add a time-independent parameter $C_{\lambda,a}$ to ensure that $\lambda_a = 0$ at the initial time. The potential \mathcal{P}_h then generates an additional force

$$-\frac{\partial \mathcal{P}_h}{\partial \mathbf{x}_a} = - \sum_b m_a m_b c_p^2 \frac{\lambda_a + \lambda_b}{\rho_0^2} h \frac{\partial \nabla w_{ab}}{\partial h}$$

so that the updated balance of momentum reads

$$\begin{aligned} \dot{\mathbf{v}}_a &= \sum_b m_b (\mathbb{T}_a + \mathbb{T}_b) \nabla w_{ab} \\ &\quad - \sum_b m_b c_p^2 \frac{\lambda_a + \lambda_b}{\rho_0^2} \frac{h}{r_{ab}} \frac{\partial^2 w_{ab}}{\partial r_{ab} \partial h} \mathbf{x}_{ab}. \end{aligned} \quad (21)$$

Restricting ourselves to the Wendland's kernel (2), we can provide these explicit formulas:

$$h \frac{\partial w}{\partial h} = \begin{cases} \frac{7}{4\pi h^2} \left(1 - \frac{r}{2h}\right)^3 \left(7 \left(\frac{r}{h}\right)^2 - \frac{3r}{h} - 2\right) & r \leq 2h \\ 0 & r \geq 2h \end{cases},$$

$$\frac{h}{r} \frac{\partial^2 w}{\partial r \partial h} = \begin{cases} -\frac{35}{4\pi h^4} \left(1 - \frac{r}{2h}\right)^2 \left(\frac{7r}{h} - 8\right) & r \leq 2h \\ 0 & r \geq 2h \end{cases}$$

in 2D, and

$$h \frac{\partial w}{\partial h} = \begin{cases} \frac{21}{32\pi h^3} \left(1 - \frac{r}{2h}\right)^3 \left(16 \left(\frac{r}{h}\right)^2 - \frac{9r}{h} - 6\right) & r \leq 2h \\ 0 & r \geq 2h \end{cases},$$

$$\frac{h}{r} \frac{\partial^2 w}{\partial r \partial h} = \begin{cases} -\frac{105}{16\pi h^5} \left(1 - \frac{r}{2h}\right)^2 \left(\frac{4r}{h} - 5\right) & r \leq 2h \\ 0 & r \geq 2h \end{cases}$$

in 3D.

From the graphs in Figure 1, we can intuitively understand the behavior of artificial force in (21) as follows: for evenly distributed particles (such as in a grid), λ_a will be close to zero, since this is the average value of $h \frac{\partial w}{\partial h}$ inside

the ball of radius $2h$ (or disc in 2D). However, λ_a will be negative when the particle a is found in a cluster or chain of particles surrounded by a void. This activates the artificial force, whose magnitude is proportional to $\frac{h}{r} \frac{\partial^2 w}{\partial r \partial h}$. This makes it strongly repulsive for nearby particles and slightly attractive for relatively large separations within the particle's sphere of influence. Thus, we get a modification of the equations similar to Monaghan's anti-clump term but with the additional benefit that the energy is conserved, albeit in a modified form, and, as we will see in the next section, the contribution of \mathcal{P}_h to the total energy is usually small.

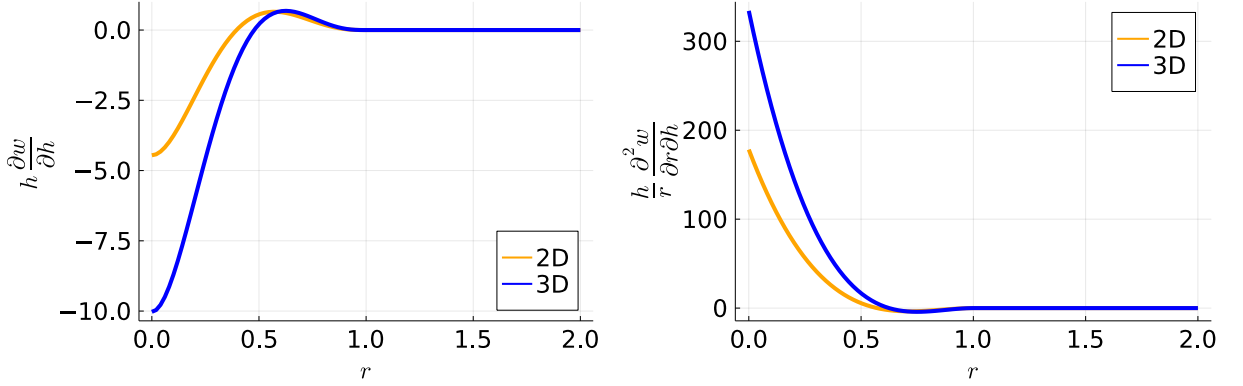


Figure 1: The plot of $h \frac{\partial w}{\partial h}$ (left) and $\frac{h}{r} \frac{\partial^2 w}{\partial r \partial h}$ (right) in two and three dimensions for $h = 1$.

3.6. Time integrator

So far, we have only been concerned with the spatial semi-discretization (discrete space, continuous time), and a time integrator is required to solve the SHTC-SPH ordinary differential equations (ODE). ODE system (12) conserve energy, and we would like to find a time integrator that preserves this property. First, let us write the system in a more succinct form:

$$\begin{aligned} \dot{\mathbf{x}}_a &= \mathbf{v}_a, \\ \dot{\mathbf{v}}_a &= \frac{\mathbf{f}_a}{m_a}, \\ \dot{\mathbb{A}}_a &= -\mathbb{A}_a \mathbb{L}_a, \end{aligned} \tag{22}$$

where the force

$$\begin{aligned} \mathbf{f}_a &= \sum_b m_a m_b \left(\mathbb{T}_a(\mathbf{x}, \rho, \mathbb{A}) + \mathbb{T}_b(\mathbf{x}, \rho, \mathbb{A}) \right) \nabla w_{ab} \\ &\quad - \sum_b m_a m_b c_p^2 \frac{\lambda_a + \lambda_b}{\rho_0^2} \frac{h}{r_{ab}} \frac{\partial^2 w_{ab}}{\partial r_{ab} \partial h} \mathbf{x}_{ab}. \end{aligned}$$

depends on \mathbf{x} , \mathbb{A} , ρ and λ . However, from equations (4), (20), we see that ρ and λ are themselves merely functions of \mathbf{x} , and thus we have $\mathbf{f}_a = \mathbf{f}_a(\mathbf{x}, \mathbb{A})$. For the discrete velocity gradient, we can write $\mathbb{L}_a = \mathbb{L}_a(\mathbf{x}, \mathbf{v})$.

Naturally, we would like to use a symplectic integrator, such as the Verlet scheme, which has excellent energy-conservation properties [20]. Unfortunately, our system is not symplectic, due to the presence of variable \mathbb{A}_a . Instead,

we suggest the following combination of Verlet (for \mathbf{x} and \mathbf{v}) and the mid-point rule (for \mathbb{A}):

$$\begin{aligned}
 \mathbf{v}_a \left(t_{k+\frac{1}{2}} \right) &= \mathbf{v}_a(t_k) + \frac{\delta t}{2m_a} \mathbf{f}_a(t_k), \\
 \mathbf{x}_a \left(t_{k+\frac{1}{2}} \right) &= \mathbf{x}_a(t_k) + \frac{\delta t}{2} \mathbf{v}_a \left(t_{k+\frac{1}{2}} \right), \\
 \mathbb{A}_a(t_{k+1}) &= \mathbb{A}_a(t_k) \left(\mathbb{I} - \frac{\delta t}{2} \mathbb{L}_a \left(t_{k+\frac{1}{2}} \right) \right) \left(\mathbb{I} + \frac{\delta t}{2} \mathbb{L}_a \left(t_{k+\frac{1}{2}} \right) \right)^{-1}, \\
 \mathbf{x}_a(t_{k+1}) &= \mathbf{x}_a \left(t_{k+\frac{1}{2}} \right) + \frac{\delta t}{2} \mathbf{v}_a \left(t_{k+\frac{1}{2}} \right), \\
 \mathbf{v}_a(t_{k+1}) &= \mathbf{v}_a \left(t_{k+\frac{1}{2}} \right) + \frac{\delta t}{2m_a} \mathbf{f}_a(t_{k+1}),
 \end{aligned} \tag{23}$$

where $t_k = k \delta t$ denotes the k -th time-step, and $\mathbf{f}_a(t)$, $\mathbb{L}_a(t)$ is a shorthand notation for

$$\mathbf{f}_a(t) = \mathbf{f}_a(\mathbf{x}(t), \mathbb{A}(t)), \quad \mathbb{L}_a(t) = \mathbb{L}_a(\mathbf{x}(t), \mathbf{v}(t)).$$

From the practical standpoint, this scheme is explicit in the sense that there are no linear or non-linear systems to be solved, or matrices to be inverted, except those of size $d \times d$. The main motivation for using (23) is to obtain discrete time-reversibility as in [21]. Indeed, inverting the sign of \mathbf{v}_a and \mathbb{L}_a in (23), we get the exactly same set of equations with the swapped role of t_k and t_{k+1} .

3.7. Adding relaxation

We now have a discrete system for elastic solid in terms of arrays \mathbf{x} , \mathbf{v} , \mathbb{A} , which constitutes the reversible part of SHTC framework. The last step is adding fluidity to our model by relaxing \mathbb{A} , and hence tangential stresses. Let us return to semi-discrete differential system (22), where we add relaxation as¹

$$\dot{\mathbf{x}}_a = \mathbf{v}_a, \tag{24a}$$

$$\dot{\mathbf{v}}_a = \frac{\mathbf{f}_a}{m_a}, \tag{24b}$$

$$\dot{\mathbb{A}}_a = -\mathbb{A}_a \mathbb{L}_a - \frac{3}{\tau c_s^2} \epsilon_{\mathbb{A}_a}, \tag{24c}$$

where τ is the *relaxation time* (noting that the potential equilibrium of \mathbb{A} is $\mathbb{A} = \mathbb{Q}$ with \mathbb{Q} being an orthogonal matrix). For an elastic solid $\tau = \infty$ and for a Newtonian fluid τ is a constant, while for non-Newtonian fluids and elastoplastic solids it should be taken as a function of \mathbb{A}_a [32, 31]. With this new addition, the equation for \mathbb{A}_a is often stiff, and therefore, implicit and exponential time integrators are recommended [10, 4]. However, we already have a very small time step in our explicit SHTC-SPH integrator (as opposed to fully implicit finite element or finite volume approaches), so for performance reasons, we use a simpler splitting strategy, using the classical RK4 scheme [20] for integrating the relaxation term in the PDE for \mathbb{A}_a :

$$\mathbf{v}_a \left(t_{k+\frac{1}{2}} \right) = \mathbf{v}_a(t_k) + \frac{\delta t}{2m_a} \mathbf{f}_a(t_k), \tag{25a}$$

$$\mathbf{x}_a \left(t_{k+\frac{1}{2}} \right) = \mathbf{x}_a(t_k) + \frac{\delta t}{2} \mathbf{v}_a \left(t_{k+\frac{1}{2}} \right), \tag{25b}$$

$$\mathbb{A}_a^*(t_k) = \mathbb{A}_a(t_k) \left(\mathbb{I} - \frac{\delta t}{2} \mathbb{L}_a \left(t_{k+\frac{1}{2}} \right) \right) \left(\mathbb{I} + \frac{\delta t}{2} \mathbb{L}_a \left(t_{k+\frac{1}{2}} \right) \right)^{-1}, \tag{25c}$$

$$\mathbb{A}_a(t_{k+1}) = \mathbb{A}_a^*(t_{k+1}) + \frac{\delta t}{6} \left(\mathbb{K}_{1,a}(t_k) + 2\mathbb{K}_{2,a}(t_k) + 2\mathbb{K}_{3,a}(t_k) + \mathbb{K}_{4,a}(t_k) \right), \tag{25d}$$

$$\mathbf{x}_a(t_{k+1}) = \mathbf{x}_a \left(t_{k+\frac{1}{2}} \right) + \frac{\delta t}{2} \mathbf{v}_a \left(t_{k+\frac{1}{2}} \right), \tag{25e}$$

¹The function θ in (1c) is taken as $\theta = \frac{\tau c_s^2}{3} (\det \mathbb{A})^{-5/3}$, see [10]. However, we omit the factor $(\det \mathbb{A})^{-5/3}$ in this paper for simplicity because it is important only in the case of compressible viscous fluids which we shall not consider here.

$$\mathbf{v}_a(t_{k+1}) = \mathbf{v}_a\left(t_{k+\frac{1}{2}}\right) + \frac{\delta t}{2m_a} \mathbf{f}_a(t_{k+1}), \quad (25f)$$

where

$$\mathbb{K}_{i,a}(t_k) = -\frac{3}{\tau c_s^2} \epsilon_{\mathbb{A}_a} \Big|_{\mathbb{A}=\mathbb{A}^*(t_k)+b_i \delta t \mathbb{K}_{i-1,a}(t_k)}, \quad i = 1, 2, 3, 4$$

and $(b_1, b_2, b_3, b_4) = (1, \frac{1}{2}, \frac{1}{2}, 1)$. Therefore, we get relatively cheap time steps and for $\tau = \infty$ (no relaxation) the scheme reduces to the reversible one (23).

Since positions are updated twice per step, we also require two neighbor list calculations in each iteration of (23).

4. Numerical results

As we have introduced the new SHTC-SPH numerical scheme, the following section contains the numerical results for both fluids and solids to demonstrate the robustness of the proposed SHTC-SPH approach. For a list of all the material and SPH parameters used in different test cases, we refer to Table 1.

4.1. Beryllium plate

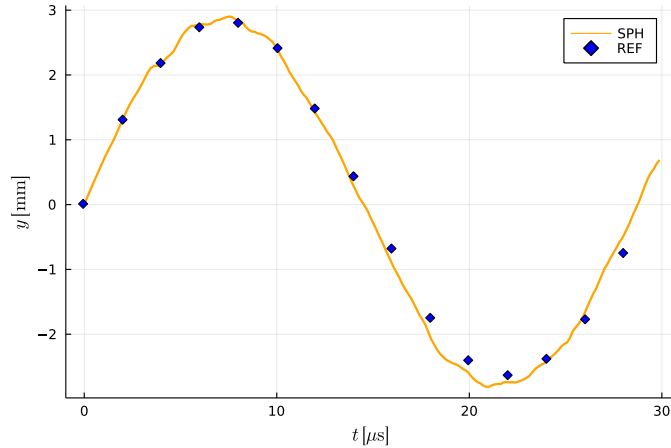


Figure 2: The y coordinate of center point in beryllium plate benchmark plotted against time. Orange line depicts the result of our scheme. Blue squares mark the referential solution.

This benchmark examines the two-dimensional oscillation of an elastic solid that is bending due to a velocity field prescribed at $t = 0$. The body in question is a translationally symmetric plate, whose cross section is a rectangle

$$\Omega = \left(-\frac{L}{2}, \frac{L}{2}\right) \times \left(-\frac{W}{2}, \frac{W}{2}\right)$$

with values $L = 0.06$ m and $W = 0.01$ m. The initial velocity field in this cross section is

$$\mathbf{v} = A\omega \begin{pmatrix} 0 \\ a_1 (\sinh s + \sin s) - a_2 (\cosh s + \cos s) \end{pmatrix}$$

where $s = \alpha \left(x + \frac{L}{2}\right)$ and $A, \omega, a_1, a_2, \alpha$ are constants with values (parameters retrieved from [4]):

$$A = 4.3369 \cdot 10^{-5} \text{ m,}$$

$$\omega = 2.3597 \cdot 10^5 \text{ s}^{-1},$$

$$\alpha = 78.834,$$

$$a_1 = 56.6368,$$

$$a_2 = 57.6455.$$

	model	δr	δt	c_0	c_s	c_p	h
Beryllium plate	DPR	2.50E-04	9.05E-10	9.05E+03	9.05E+03	9.05E+04	3.75E-04
Twisting column	NH	4.96E-02	3.44E-06	7.15E+02	7.19E+01	7.15E+03	7.44E-02
Taylor-Couette flow	DPR	3.33E-02	3.31E-05	2.00E+01	4.00E+01	2.00E-01	5.00E-02
Lid-driven cavity, Re 100	DPR	5.00E-03	1.50E-05	2.00E+01	2.00E+01	0.00E+00	7.50E-03
Lid-driven cavity, Re 400	DPR	7.14E-03	1.50E-05	2.00E+01	2.00E+01	0.00E+00	1.07E-02

Table 1

Summary of simulation parameters used in this paper.

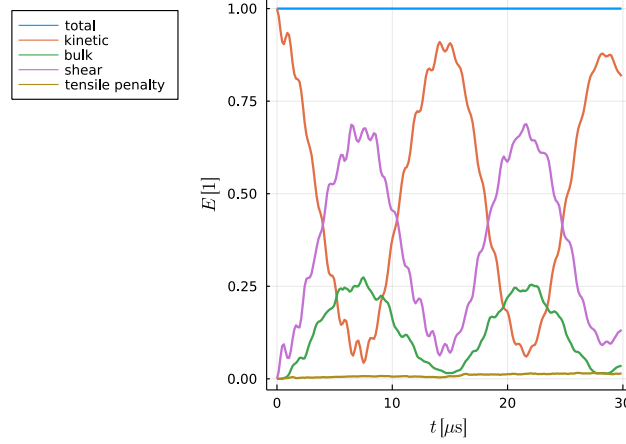


Figure 3: Different contributions to energy in beryllium plate benchmark plotted against time, normalized. Interestingly, the tensile penalty contribution is kept relatively small despite its profound importance in the evolution.

We use the constitutive relation (13)-(15) for with

$$c_0 = c_s = 9046.59 \text{ m s}^{-1}.$$

Complete elasticity is assumed and therefore $\tau = \infty$. We choose the spatial step $\delta r = W/40$ which gives us approximately 10000 particles. The time step is selected according to

$$\delta t = \frac{0.05\delta r}{\sqrt{c_0^2 + \frac{4}{3}c_s^2}} \quad (26)$$

and the simulation ends at time $t = 3 \cdot 10^{-5}$ s, roughly corresponding to one period of the oscillating motion.

Three things can be tested in this benchmark. Firstly, we plot the y coordinate of the central point, which we then compare to data from the finite volume simulation [4]. Figure 2 shows that we get a reasonable agreement. Second, since there are no dissipative or external forces involved, it presents an ideal test for verifying the conservation of energy, which we achieve to a reasonable degree, see Figure 3. Last but not least, due to the presence of strongly negative pressures, this simulation poses a challenge with respect to tensile instability, demonstrating the usefulness of the penalty term (19). In fact, without this addition, the plate would tear completely as can be seen in Figure 4.

4.2. Twisting column

The next benchmark is borrowed from [19]. The initial setup is a cuboid

$$\Omega = \left(-\frac{W}{2}, \frac{W}{2}\right) \times \left(-\frac{W}{2}, \frac{W}{2}\right) \times (0, H) \quad (27)$$

where $W = 1\text{m}$ and $H = 6\text{m}$ which is subjected to a prescribed velocity field

$$\mathbf{v} = \omega \sin\left(\frac{\pi z}{2H}\right) \begin{pmatrix} y \\ -x \\ 0 \end{pmatrix},$$

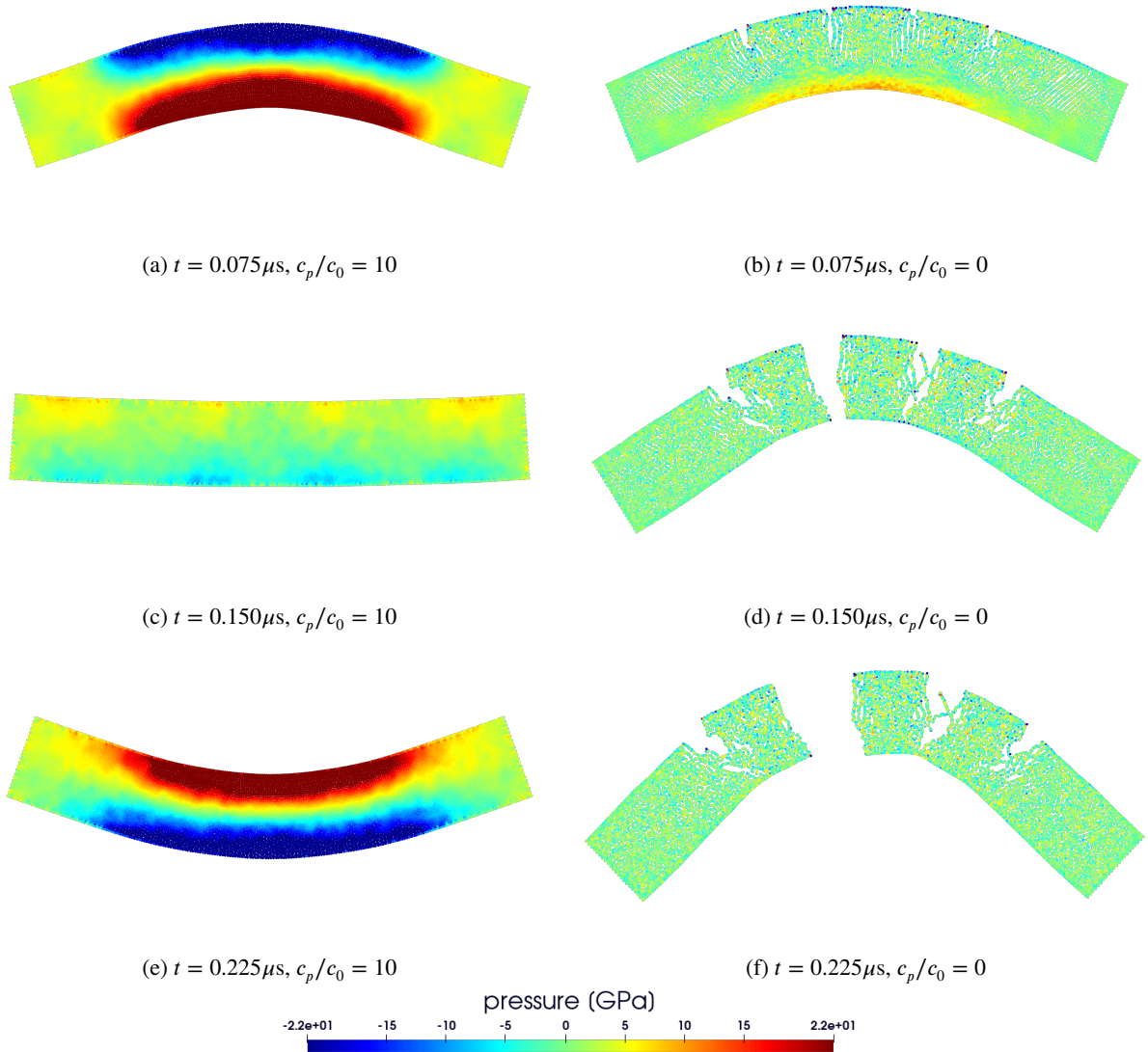


Figure 4: Images of beryllium plate simulation and color-plot for pressure with tensile instability treatment (left) and without (right). For $c_p = 0$, particles have an extra degree of freedom which allows them to minimize negative pressure by forming clumps. This results in clearly non-physical behavior.

where $\omega = 105 \text{ s}^{-1}$. The base of the column is kept in place by a Dirichlet boundary condition for velocity. Here, we use the fully elastic ($\tau = \infty$) Neo-Hookean model (17) with $\rho_0 = 1100 \text{ kg/m}^3$, $Y = 17 \text{ MPa}$ (Young modulus), $\nu = 0.495$ (Poisson ratio). These values are related to the bulk shear sound speed by relations:

$$\rho_0 c_s^2 = \frac{Y}{1 + \nu}, \quad \rho_0 c_0^2 = \frac{\nu Y}{(1 + \nu)(1 - 2\nu)}.$$

In this benchmark, inertia should twist the column, building up tensile forces that eventually prevail and reverse the rotation. The shape of the column should recover without loss of energy. Additionally, there is associated non-linear effect, which causes shrinkage of the column. All these phenomena are observed in our simulation, as can be seen in Figures 5, 7. We still have reasonably good energy conservation (Figure 6), but the Dirichlet boundary condition at the base is slightly dissipative (since it is implemented by resetting the velocity to zero at every time step). Unfortunately,

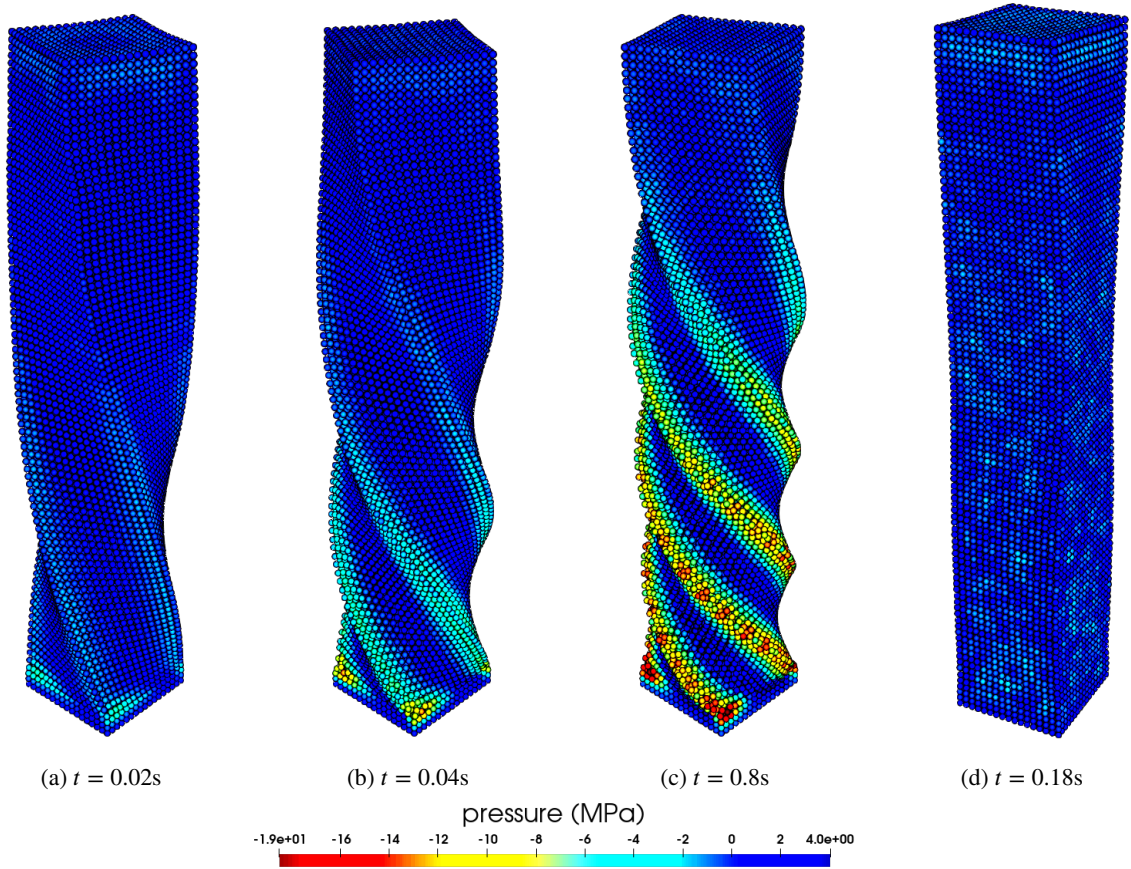


Figure 5: Result of the twisting column simulation with a color-plot for pressure. We use this as a qualitative test whether our code can deal with large elastic deformations in three dimensions. The last frame shows the column after untwisting, showing some noise in the pressure field (presumably, this can be remedied by adding artificial dissipation). Shape of the column is not exactly recovered but note that the elastic energy is not perfectly zero at this point either (see Figure 6).

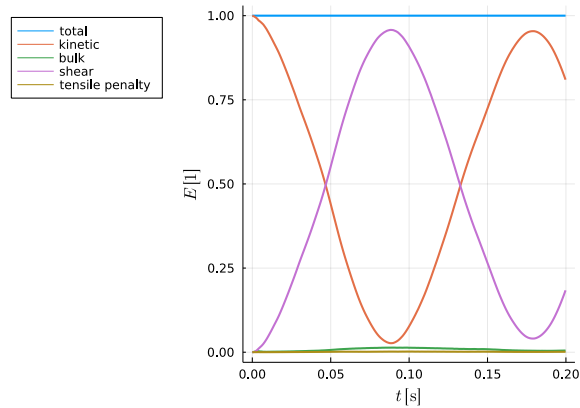


Figure 6: Energy conservation in twisting column benchmark.

variables like pressure become very noisy in the simulation after a short time, but we did not find a remedy which would not involve artificial dissipation.

SHTC-SPH

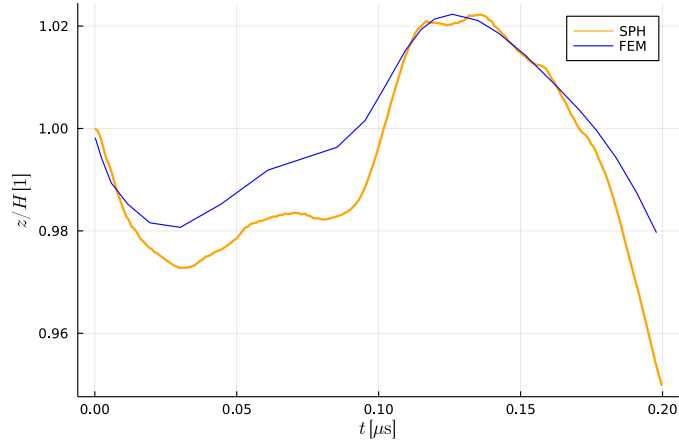


Figure 7: Twisting column: the normalized z -coordinate of material point initially at $(0, 0, H)$ plotted against time. Although the column is shrinking at first, it “bounces off” at some point and starts to elongate. This effect was also observed in [4] and [19]. The blue line shows comparison to a finite element simulation (created using the Fenics software [23]).

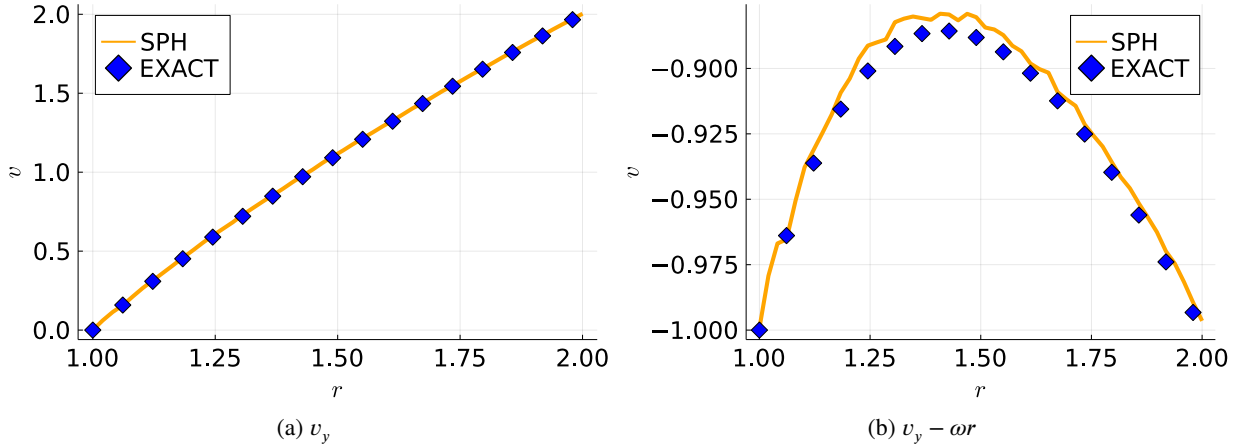


Figure 8: Tangential velocity in the simulation at $t = 10$ along the segment $y = 0$, $R_1 \leq x \leq R_2$ (orange line) and its comparison to the exact solution (blue squares). Picture on the right magnifies error by subtracting a linear approximation $v_y \approx \omega r$ from both data arrays.

4.3. Laminar Taylor-Couette flow

We now turn our attention to the fluid regime of the SHTC equations, which means that $\tau < \infty$ and the relaxation terms need to be taken into account. First, we try a simple test of laminar flow in an annulus

$$\Omega = \{(x, y) : R_1^2 < x^2 + y^2 < R_2^2\}$$

driven by a rigid counterclockwise rotation of the outer ring with angular velocity ω . Meanwhile, the inner ring has zero angular velocity. We take $R_1 = 1$, $R_2 = 2$ and $\omega = 1$. The flow is incompressible and well described by the incompressible Navier-Stokes equations with kinetic viscosity $\nu = 0.1$. This corresponds to a low Reynolds number

$$\text{Re} = \frac{\omega R_2 (R_2 - R_1)}{\nu} = 20,$$

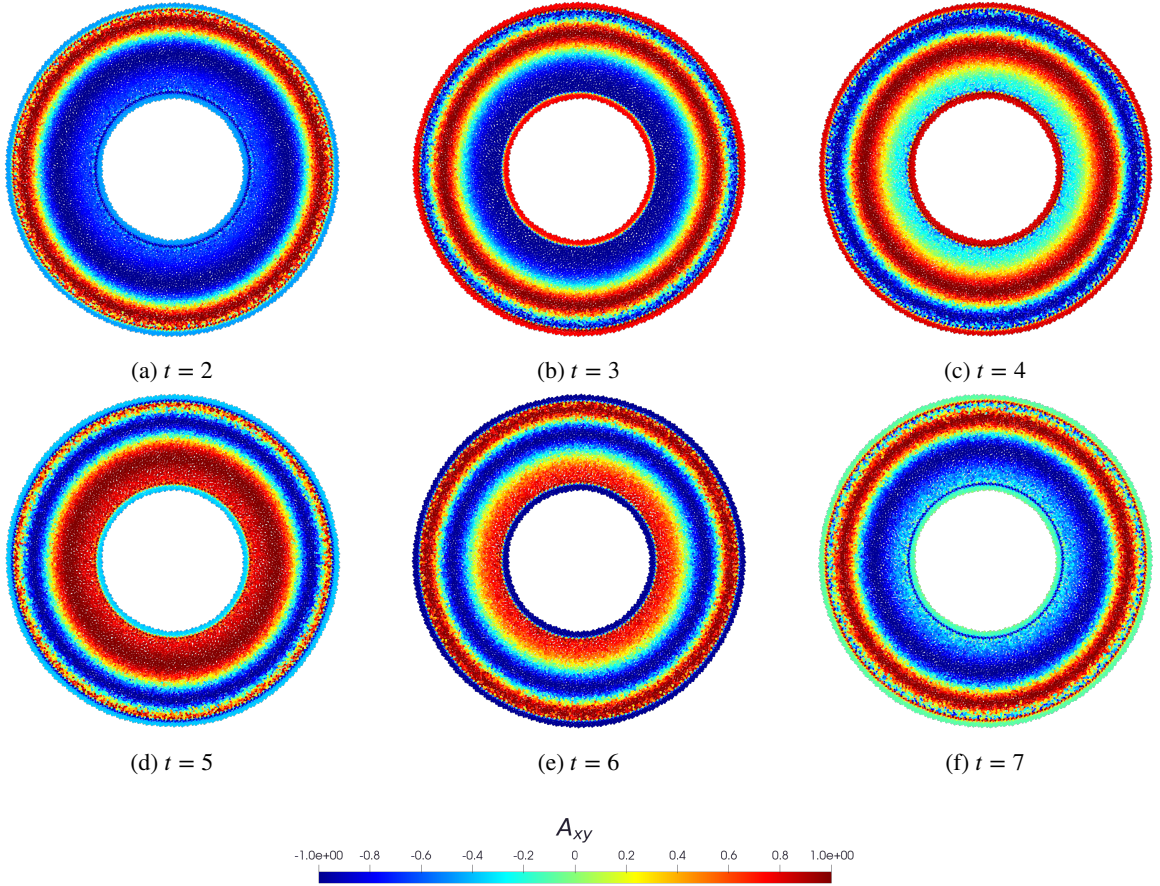


Figure 9: Plot of xy distortion component. Interestingly, whereas velocity converges in time (approximately) to the stationary solution (28), the A field is always changing in a periodic manner, forming waves that travel from the outer ring towards the center.

which ensures laminar flow. The exact stationary solution to this problem is given by the formula

$$\mathbf{v} = \frac{R_2}{r} \frac{\frac{r}{R_1} - \frac{R_1}{r}}{\frac{R_2}{R_1} - \frac{R_1}{R_2}} \begin{pmatrix} -\omega y \\ \omega x \end{pmatrix}. \quad (28)$$

The solution theoretically does not depend on ν but viscosity affects how quickly the velocity field converges (if at all), starting from $\mathbf{v} = \mathbf{0}$.

The Navier-Stokes equations (NSEs) are formally incompatible with the SHTC equations, which can be inferred from the fact that NSEs are a hyperbolic-parabolic system, whereas SHTC equations include only first-order hyperbolic equations. However, it is possible to obtain NSEs (at least formally) in the asymptotic expansion of the SHTC equations as the first-order terms in τ [10]. To achieve sufficiently small values of τ one needs to take sufficiently large values of the shear sound speed since they are related as [10]

$$\tau = \frac{6\nu}{c_s^2}. \quad (29)$$

Here, we essentially mirror the common approach in SPH, where incompressibility is enforced by “sufficiently high” values of c_0 (corresponding to small Mach number $\text{Ma} = \|\mathbf{v}\|/c_0 \ll 1$) but this time for the shear component of energy.

The characteristic speed in this simulation is $\omega R_2 = 2$, so it is reasonable to take $c_0 = 20$ and $c_s = 40$. Here, we set $\delta r = \frac{1}{40}$ and δt according to (26). With these parameters, we get

$$\frac{\delta t}{\tau} \doteq 0.075$$

so the natural time step is significantly smaller than τ , justifying the use of an explicit time integrator for relaxation.

Despite the numerous approximations used, we obtain reasonable agreement with the exact solution, as shown in Figure 8. It is interesting here to plot the distortion field (Figure 9). Even for such a simple *stationary* flow, \mathbb{A} displays non-stationary behavior due to the rotation of the local basis vectors represented by \mathbb{A} , e.g. see [32, 10, 34].

4.4. Lid-driven cavity (Newtonian fluid)

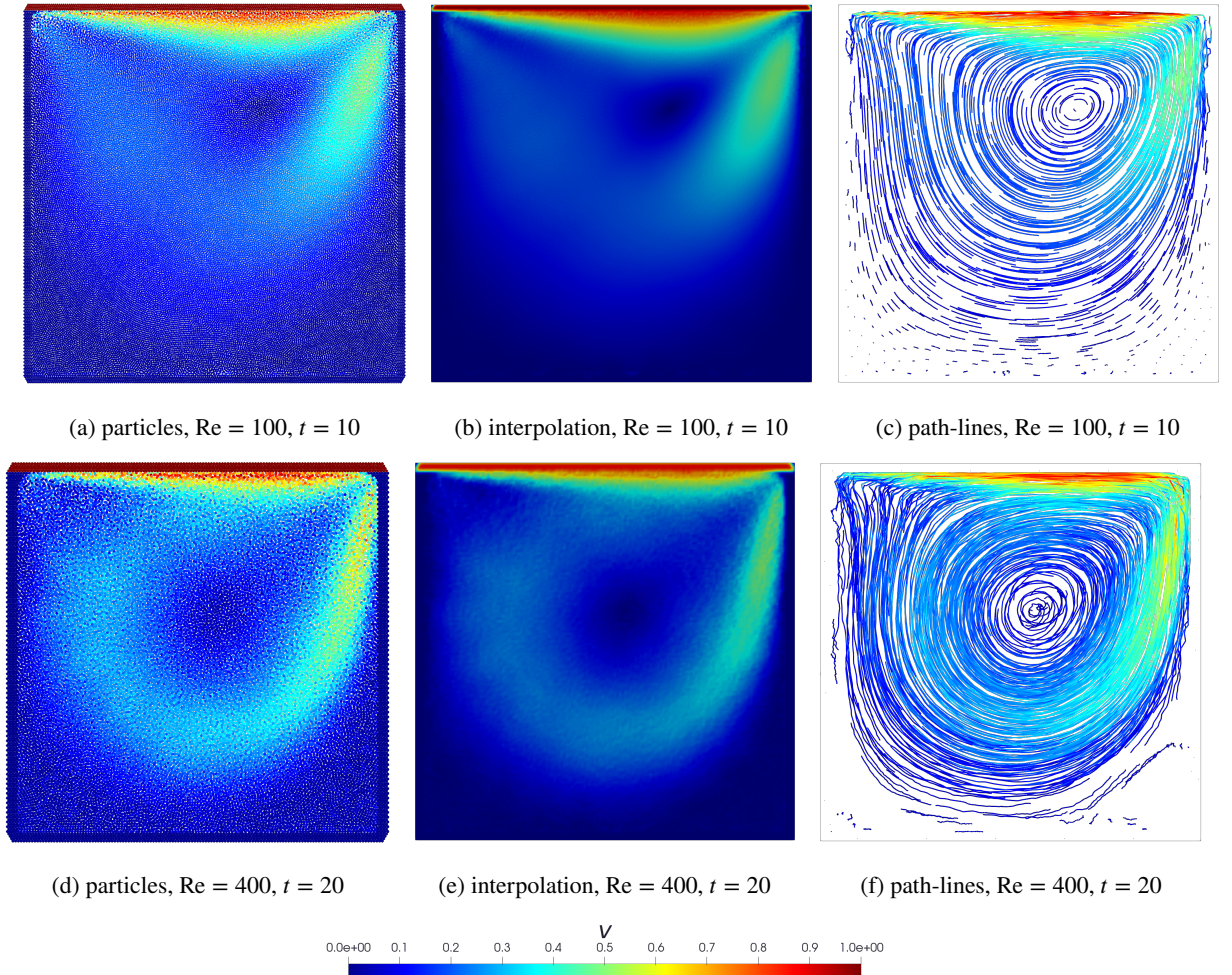


Figure 10: Velocity field in the Newtonian lid-driven cavity benchmark.

The advantages of the Taylor-Couette benchmark are simple implementation and availability of an exact solution (in steady state at least). It is, however, insufficient in the sense that the velocity field does not depend on the magnitude of v . For a more qualitative and challenging test, we include the lid-driven cavity benchmark. The geometry of this problem consists of a square $\Omega = (0, 1) \times (0, 1)$ filled with a viscous fluid. The left, right, and bottom boundaries are

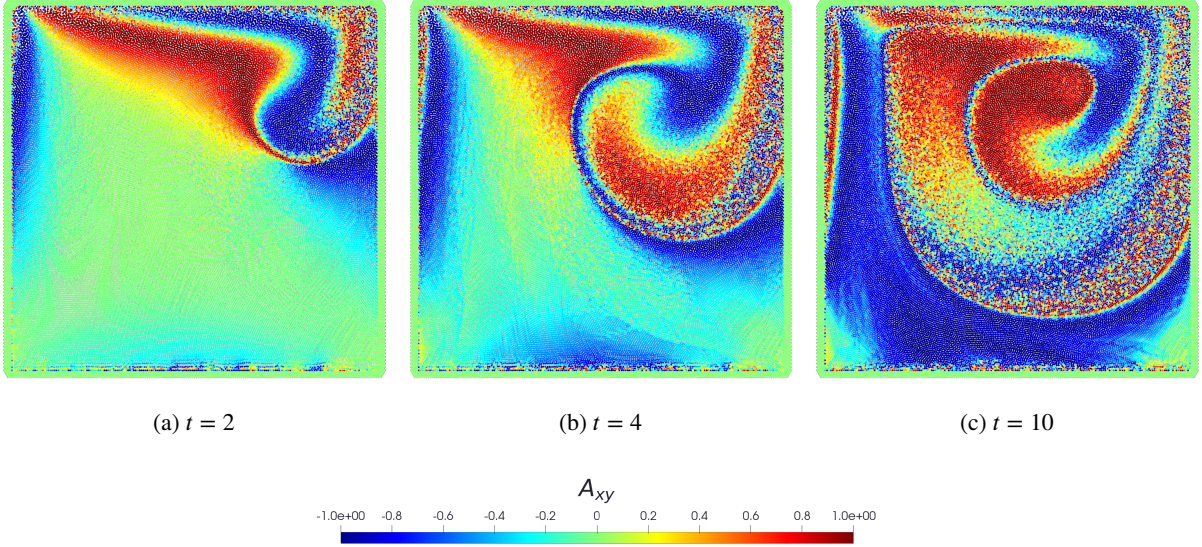


Figure 11: Evolution of distortion field in Newtonian lid-driven cavity benchmark for $\text{Re} = 100$.

the walls with a no slip boundary condition, i.e. $\mathbf{v} = 0$, and the top boundary is moving at the prescribed velocity

$$\mathbf{v}_{\text{lid}} = \begin{pmatrix} 1 \\ 0 \end{pmatrix}.$$

For the shear energy, we use the constitutive equation (15) with $\rho = 1$. Again, in the case of fluid flows, and especially incompressible flows, the ideal values for the shear and bulk speed of sound would be $c_s \gg 1$, $c_0 \gg 1$ corresponding to the incompressible Navier-Stokes limit of the SHTC equations, i.e. $\tau \sim \nu/c_s^2 \ll 1$ and $\text{Ma} \sim \|\mathbf{v}\|/c_0 \ll 1$, but this is not possible in our scheme because the underlying ODE system (24) would become extremely stiff. Therefore, as an approximation, we set²

$$c_s = c_0 = 20.$$

We consider the cases of $\text{Re} = 100$ and $\text{Re} = 400$. The viscosity and the relaxation time are related to this number by:

$$\nu = \frac{1}{\text{Re}}, \quad \tau = \frac{6\nu}{c_s^2}.$$

The no slip walls are implemented as h -deep layer of particles with zero velocity. The lid is implemented similarly with immobile particles but “pretending” to have velocity \mathbf{v}_{lid} for the purposes of \mathbb{L} computation (equation (7)). The initial state is somewhat problematic in a weakly compressible scheme because discontinuities in the velocity field will generate shock waves. For this reason, we fix the zero lid velocity at $t = 0$ and gradually accelerate it up to 1.

The results are shown in Figures 10, 11. In Figure 12, we plot the transverse velocity along the center lines and compare the result to a referential solution [13]. Despite one can see slight discrepancies between SPH-SHTC solution and the reference one in Figure 12 (which we suspect is caused by the problematic implementation of the Dirichlet boundary condition) a reasonable agreement between the solutions has been achieved.

²We note that the shear sound speed c_s is not an artificial fitting parameter in the SHTC equations but it can be measured for real fluids via the sound dispersion data and fitted via a procedure described in [9].

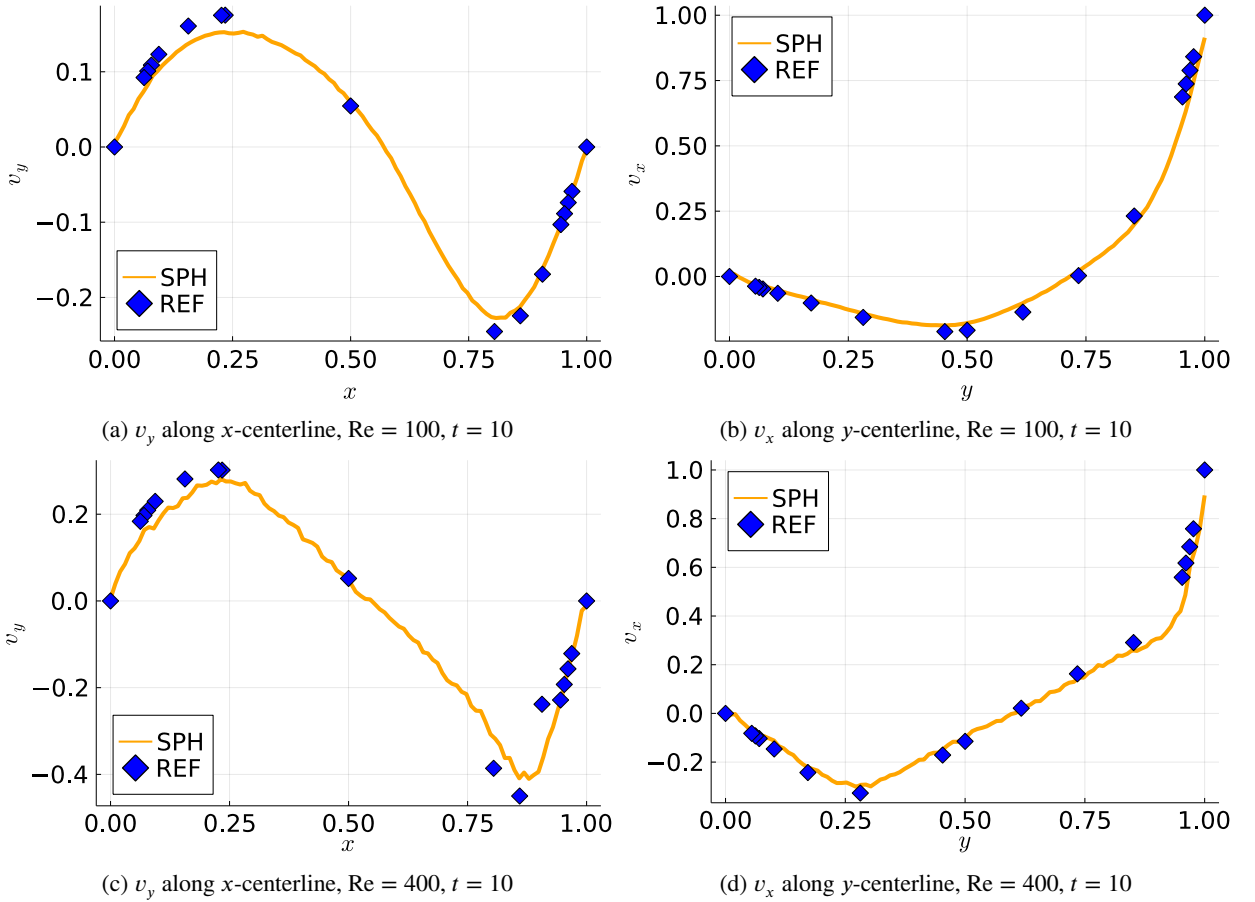


Figure 12: Plot of transverse velocities along lines $x = \frac{1}{2}$ and $y = \frac{1}{2}$ in the Newtonian lid-drive cavity benchmark.

5. Conclusion

We have developed a new SHTC-SPH numerical method that is suitable for simulations of both fluids and solids within a single framework. To the best of our knowledge it is the first ever discretization of the SHTC equations with an SPH scheme. The method discretizes (both in space and time) the Symmetric Hyperbolic Thermodynamically Compatible equations (1), which describe both fluids and solids. First, we discretize them in space, which results in the SHTC-SPH ordinary differential equations (12), which contain an evolution equation for a discrete analogue of the distortion field. Then, we prescribe a time integrator (23), which gives the SHTC-SPH numerical scheme.

The scheme is then tested on benchmarks like a vibrating Beryllium plate, twisting column, laminar Taylor-Couette flow, and lid-driven cavity flow, and shows acceptable agreement with the data, although finite volume and discontinuous Galerkin ADER schemes [10, 4] usually offer better precision.

In the future, we would like to investigate deeper geometrical properties of the SHTC-SPH scheme, such as its Hamiltonianity and conservation of Casimirs [30] as well as incorporating the heat conduction part of the SHTC equations. In addition, we plan to combine SHTC with the implicit variant of SPH for improved stability and performance.

Acknowledgments

The authors are grateful to Markus Huetter for bringing our attention to the paper by Falk and Langer which helped us to construct the proposed discretization of the distortion field. OK was supported by project No. START/SCI/053 of Charles University Research program. MP was supported by project No. UNCE/SCI/023 of Charles University Research program. OK, MP and VK were also supported by the Czech Science Foundation (project no. 20-22092S). IP

is a member of the Gruppo Nazionale per il Calcolo Scientifico of the Istituto Nazionale di Alta Matematica (INdAM GNCS) and acknowledges the financial support received from the Italian Ministry of Education, University and Research (MIUR) in the frame of the Departments of Excellence Initiative 2018–2022 attributed to the Department of Civil, Environmental and Mechanical Engineering (DICAM) of the University of Trento (Grant No. L.232/2016) and in the frame of the Progetti di Rilevante Interesse Nazionale (PRIN) 2017, Project No. 2017KKJP4X, “Innovative numerical methods for evolutionary partial differential equations and applications”.

References

- [1] Andreotti, B., Forterre, Y., Pouliquen, O., 2013. *Granular Media: Between Fluid and Solid*. Cambridge University Press. URL: <http://www.edition-sciences.com/milieux-granulaires-entre-fluide-et-solide.htm>, doi:10.1080/00107514.2014.885579.
- [2] Antoci, C., Gallati, M., Sibilla, S., 2007. Numerical simulation of fluid–structure interaction by sph. *Computers & structures* 85, 879–890.
- [3] Bonet, J., Lok, T.S., 1999. Variational and momentum preservation aspects of smooth particle hydrodynamic formulations. *Computer Methods in applied mechanics and engineering* 180, 97–115.
- [4] Boscheri, W., Chiocchetti, S., Peshkov, I., 2022. A cell-centered implicit-explicit Lagrangian scheme for a unified model of nonlinear continuum mechanics on unstructured meshes. *Journal of Computational Physics* 451, 110852. URL: <http://arxiv.org/abs/2107.06038https://linkinghub.elsevier.com/retrieve/pii/S0021999121007476https://doi.org/10.1016/j.jcp.2021.110852>, doi:10.1016/j.jcp.2021.110852, arXiv:2107.06038.
- [5] Boscheri, W., Dumbser, M., Ioriatti, M., Peshkov, I., Romenski, E., 2021. A structure-preserving staggered semi-implicit finite volume scheme for continuum mechanics. *Journal of Computational Physics* 424, 109866. URL: <https://linkinghub.elsevier.com/retrieve/pii/S0021999120306409>, doi:10.1016/j.jcp.2020.109866, arXiv:2005.04296.
- [6] Brazhkin, V.V., Fomin, Y.D., Lyapin, A.G., Ryzhov, V.N., Trachenko, K., 2012. Two liquid states of matter: A dynamic line on a phase diagram. *Physical Review E* 85, 031203. URL: <https://link.aps.org/doi/10.1103/PhysRevE.85.031203>, doi:10.1103/PhysRevE.85.031203.
- [7] Busto, S., Chiocchetti, S., Dumbser, M., Gaburro, E., Peshkov, I., 2020. High Order ADER Schemes for Continuum Mechanics. *Frontiers in Physics* 8. URL: <http://arxiv.org/abs/1912.01964https://www.frontiersin.org/article/10.3389/fphy.2020.00032/full>, doi:10.3389/fphy.2020.00032, arXiv:1912.01964.
- [8] Busto, S., Dumbser, M., Peshkov, I., Romenski, E., 2022. On thermodynamically compatible finite volume schemes for continuum mechanics. Accepted in *SIAM Journal on Scientific Computing*.
- [9] Dumbser, M., Peshkov, I., Romenski, E., 2018. A unified hyperbolic formulation for viscous fluids and elastoplastic solids, in: Klingenberg, C., Westdickenberg, M. (Eds.), *Springer Proceedings in Mathematics and Statistics*. Springer International Publishing, Cham. volume 237 of *Springer Proceedings in Mathematics and Statistics*, pp. 451–463. URL: http://dx.doi.org/10.1007/978-3-319-91548-7_34http://arxiv.org/abs/1705.02151http://link.springer.com/10.1007/978-3-319-91548-7_34, doi:10.1007/978-3-319-91548-7_34, arXiv:1705.02151.
- [10] Dumbser, M., Peshkov, I., Romenski, E., Zanotti, O., 2016. High order ADER schemes for a unified first order hyperbolic formulation of continuum mechanics: Viscous heat-conducting fluids and elastic solids. *Journal of Computational Physics* 314, 824–862. URL: <http://dx.doi.org/10.1016/j.jcp.2016.02.015>, doi:10.1016/j.jcp.2016.02.015, arXiv:1511.08995.
- [11] Falk, M.L., Lange, J.S., 1998. Dynamics of viscoplastic deformation in amorphous solids. *Physical Review E* 57.
- [12] Frenkel, J., 1955. *Kinetic theory of liquids*. Dover, New York, NY.
- [13] Ghia, U., Ghia, K.N., Shin, C., 1982. High-re solutions for incompressible flow using the navier-stokes equations and a multigrid method. *Journal of computational physics* 48, 387–411.
- [14] Gingold, R., Monaghan, J., 1977. Smoothed particle hydrodynamics: theory and application to non-spherical stars. *Mon. Not. R. Astron. Soc.* 181, 375–389.
- [15] Godunov, S., Romenskiy, E., 1995. Thermodynamics, conservation laws and symmetric forms of differential equations in mechanics of continuous media, in: *Computational Fluid Dynamics Review 1995*. John Wiley, NY. volume 95, pp. 19–31. doi:10.1142/7799.
- [16] Godunov, S.K., 1961. An interesting class of quasilinear systems. *Dokl. Akad. Nauk SSSR* 139(3), 521–523.
- [17] Godunov, S.K., Romenskii, E.I., 2003. *Elements of continuum mechanics and conservation laws*. Kluwer Academic/Plenum Publishers.
- [18] Grmela, M., Öttinger, H.C., 1997. Dynamics and thermodynamics of complex fluids. I. Development of a general formalism. *Phys. Rev. E* 56, 6620–6632. URL: <http://link.aps.org/doi/10.1103/PhysRevE.56.6620>, doi:10.1103/PhysRevE.56.6620.
- [19] Haider, J., Lee, C.H., Gil, A.J., Huerta, A., Bonet, J., 2018. An upwind cell centred total lagrangian finite volume algorithm for nearly incompressible explicit fast solid dynamic applications. *Computer Methods in Applied Mechanics and Engineering* 340, 684–727.
- [20] Hairer, E., Lubich, C., Wanner, G., 2013. *Geometric Numerical Integration: Structure-Preserving Algorithms for Ordinary Differential Equations*. Springer Series in Computational Mathematics, Springer Berlin Heidelberg. URL: <https://books.google.cz/books?id=cPTxCAAQBAJ>.
- [21] Kincl, O., Pavelka, M., 2022. Globally time-reversible fluid simulations with smoothed particle hydrodynamics.
- [22] Lee, C.H., Gil, A.J., Greto, G., Kulasegaram, S., Bonet, J., 2016. A new Jameson–Schmidt–Turkel Smooth Particle Hydrodynamics algorithm for large strain explicit fast dynamics. *Computer Methods in Applied Mechanics and Engineering* 311, 71–111. URL: <http://linkinghub.elsevier.com/retrieve/pii/S0045782516304182https://linkinghub.elsevier.com/retrieve/pii/S0045782516304182>, doi:10.1016/j.cma.2016.07.033.
- [23] Logg, A., Mardal, K.A., Wells, G.N., et al., 2012. *Automated Solution of Differential Equations by the Finite Element Method*. Springer. doi:10.1007/978-3-642-23099-8.
- [24] Monaghan, J., 2005. Smoothed particle hydrodynamics. *Reports on Progress in Physics* 68, 1703. doi:10.1088/0034-4885/68/8/R01.
- [25] Monaghan, J., Kocharyan, A., 1995. Sph simulation of multi-phase flow. *Computer Physics Communications* 87, 225–235.

- [26] Monaghan, J.J., 2000. Sph without a tensile instability. *Journal of computational physics* 159, 290–311.
- [27] Öttinger, H.C., Grmela, M., 1997. Dynamics and thermodynamics of complex fluids. II. Illustrations of a general formalism. *Phys. Rev. E* 56, 6633–6655. doi:10.1103/PhysRevE.56.6633.
- [28] Pavelka, M., Klika, V., Grmela, M., 2018. *Multiscale Thermo-Dynamics*. de Gruyter, Berlin.
- [29] Pavelka, M., Peshkov, I., Klika, V., 2020. On Hamiltonian continuum mechanics. *Physica D: Nonlinear phenomena* 408.
- [30] Pelech, P., Tøuma, K., Pavelka, M., Martin Šípka, M.S., 2020. On compatibility of the natural configuration framework with GENERIC: Derivation of anisotropic rate-type models.
- [31] Peshkov, I., Boscheri, W., Loubère, R., Romenski, E., Dumbser, M., 2019. Theoretical and numerical comparison of hyperelastic and hypoelastic formulations for Eulerian non-linear elastoplasticity. *Journal of Computational Physics* 387, 481–521. URL: <http://arxiv.org/abs/1806.00706><https://linkinghub.elsevier.com/retrieve/pii/S0021999119301561><https://doi.org/10.1016/j.jcp.2019.02.039>, doi:10.1016/j.jcp.2019.02.039, arXiv:1806.00706.
- [32] Peshkov, I., Dumbser, M., Boscheri, W., Romenski, E., Chiocchetti, S., Ioriatti, M., 2021. Simulation of non-Newtonian viscoplastic flows with a unified first order hyperbolic model and a structure-preserving semi-implicit scheme. *Computers & Fluids* 224, 104963. URL: <http://arxiv.org/abs/2012.07656><https://linkinghub.elsevier.com/retrieve/pii/S0045793021001304>, doi:10.1016/j.compfluid.2021.104963, arXiv:2012.07656.
- [33] Peshkov, I., Pavelka, M., Romenski, E., Grmela, M., 2018. Continuum mechanics and thermodynamics in the Hamilton and the Godunov-type formulations. *Continuum Mechanics and Thermodynamics* 30, 1343–1378. URL: <http://link.springer.com/10.1007/s00161-018-0621-2><https://arxiv.org/abs/1710.00058><https://link.springer.com/article/10.1007/s00161-018-0621-2>, arXiv:1710.00058.
- [34] Peshkov, I., Romenski, E., 2016. A hyperbolic model for viscous Newtonian flows. *Continuum Mechanics and Thermodynamics* 28, 85–104. URL: <https://link.springer.com/article/10.1007/s00161-014-0401-6><http://link.springer.com/10.1007/s00161-014-0401-6>, doi:10.1007/s00161-014-0401-6.
- [35] Romenski, E.I., 1998. Hyperbolic systems of thermodynamically compatible conservation laws in continuum mechanics. *Mathematical and computer modelling* 28, 115–130. URL: <https://www.sciencedirect.com/science/article/pii/S0895717798001599>, doi:10.1016/S0895-7177(98)00159-9.
- [36] Sun, P., Colagrossi, A., Marrone, S., Antuono, M., Zhang, A.M., 2019. A consistent approach to particle shifting in the δ -plus-sph model. *Computer Methods in Applied Mechanics and Engineering* 348, 912–934.
- [37] Vila, J., 1999. On particle weighted methods and smooth particle hydrodynamics. *Mathematical models and methods in applied sciences* 9, 161–209.
- [38] Violeau, D., 2012. *Fluid Mechanics and the SPH Method: Theory and Applications*. Oxford University Press, Oxford, UK.